Article

Exceptional point and hysteresis trajectories in cold Rydberg atomic gases

Jun Zhang[1,2,3], En-Ze Li[1,2,3], Ya-Jun Wang[1,2,3], Bang Liu[1,2], Li-Hua Zhang[1,2], Zheng-Yuan Zhang[1,2], Shi-Yao Shao[1,2], Qing Li[1,2], Han-Chao Chen[1,2], Yu Ma[1,2], Tian-Yu Han[1,2], Qi-Feng Wang[1,2], Jia-Dou Nan[1,2], Yi-Ming Yin[1,2], Dong-Yang Zhu[1,2], Guang-Can Guo[1,2], Dong-Sheng Ding ⓘ [1,2] ✉ & Bao-Sen Shi ⓘ [1,2]

The interplay between strong long-range interactions and the coherent driving contribute to the formation of complex patterns, symmetry, and novel phases of matter in many-body systems. However, long-range interactions may induce an additional dissipation channel, resulting in non-Hermitian many-body dynamics and the emergence of exceptional points in spectrum. Here, we report experimental observation of interaction-induced exceptional points in cold Rydberg atomic gases, revealing the breaking of charge-conjugation parity symmetry. By measuring the transmission spectrum under increasing and decreasing probe intensity, the interaction-induced hysteresis trajectories are observed, which give rise to non-Hermitian dynamics. We record the area enclosed by hysteresis loops and investigate the dynamics of hysteresis loops. The reported exceptional points and hysteresis trajectories in cold Rydberg atomic gases provide valuable insights into the underlying non-Hermitian physics in many-body systems, allowing us to study the interplay between long-range interactions and non-Hermiticity.

Exceptional points (EPs) are special points in the parameter space of a non-Hermitian system where two or more eigenstates and their corresponding eigenvalues coalesce. At these points, compared to the Hermitian Hamiltonian, the eigenvalues of the underlying system's Hamiltonian have complex values[1–5]. Recent studies have shown that open systems undergo phase transitions at EPs, leading to a variety of interesting physical phenomena, including chirality[6,7], unidirectional transmission or reflection[8,9], topological phase transition[10,11], parity-time symmetry breaking[12,13] and charge-conjugation parity (CP) symmetry breaking[14], and supernormal sensitivity to perturbations[15,16]. These properties have become the focus of research on non-Hermitian systems associated with EPs, which opened the door to a series of experimental studies in optics[17–20], electronics[21,22], and enhanced sensing[23–27] (where the sensor sensitivity is enhanced by energy bifurcation near the EPs). The combination between non-Hermiticity and many-body interaction enables the emergence of non-trivial effects[28–30], thus providing a platform to study the emergent phases beyond few-body scenarios.

Due to the strong dipole interaction between Rydberg atoms[31–33], they have become a versatile tool for studying many-body physics. This long-range interaction induces non-linearity and gives rise to a unique dissipation channel, enabling investigations into non-equilibrium phase transitions[34–40], self-organization[41–44], ergodicity breaking and time crystals[45–51]. The dissipation induced by interactions can cause energy to be exchanged between a many-body system and its external environment, thereby influencing the dynamics and symmetric properties of the system, i.e., non-Hermitian many-body physics. Thus, studying the relationship between many-body interactions and non-Hermiticity can provide a new framework to investigate non-Hermitian dynamics in many-body scenarios[52]. Studying these in Rydberg atom systems has advantages in precise control of interactions, offering valuable

[1]Key Laboratory of Quantum Information, University of Science and Technology of China, Hefei, Anhui, China. [2]Synergetic Innovation Center of Quantum Information and Quantum Physics, University of Science and Technology of China, Hefei, Anhui, China. [3]These authors contributed equally: Jun Zhang, En-Ze Li, Ya-Jun Wang. ✉e-mail: dds@ustc.edu.cn
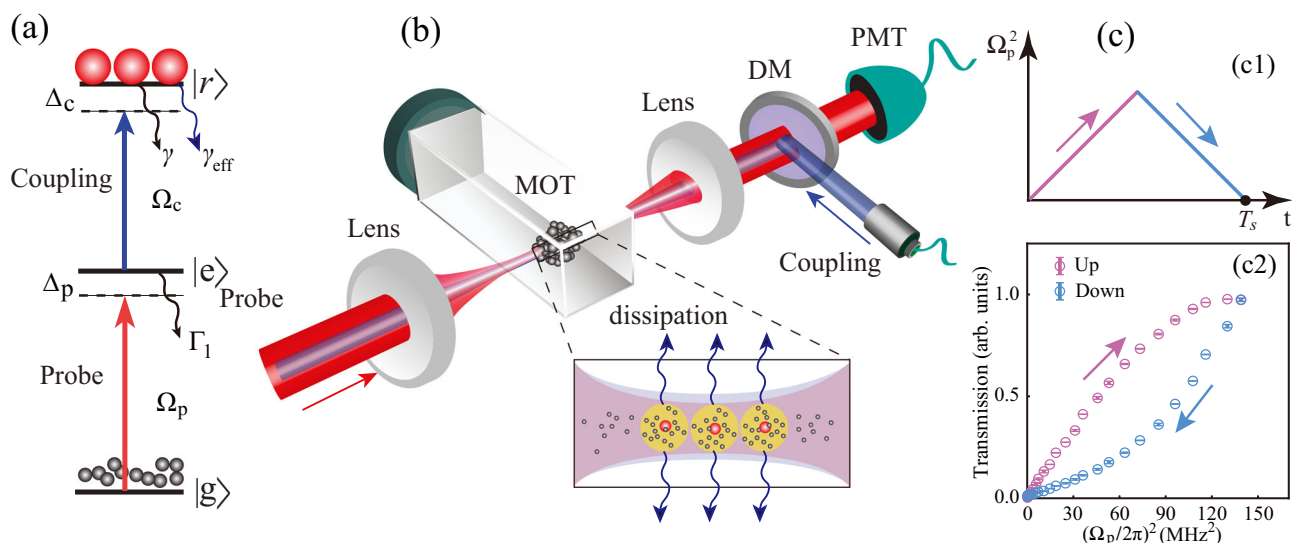
Fig. 1 | Schematic of many-body interaction induced EPs and hysteresis loops in Rydberg atoms. a Rydberg atomic energy level diagrams. Probe Ω_p and coupling Ω_c fields excite atoms with detunings Δ_p and Δ_c. Γ_1 and γ are spontaneous decay rates of states $|e\rangle$ and $|r\rangle$, and γ_{eff} is the decay rate caused by Rydberg many-body interactions. **b** Schematic diagram of the experimental setup. The probe beam is incident opposite to the coupling beam through the lens and focused in a magneto-optic trap (MOT) trapping ^{85}Rb atoms, and the transmission signals are detected using a photo-multiplier tube (PMT). **c** Measured transmission by positively (Up, pink) and negatively (Down, blue) scanning $(\Omega_p/2\pi)^2$ with the scan time T_s, and the trajectories connected by data points exhibit hysteresis loop.

insights in finding new emergent phases in symmetry breaking[14], which is the starting point of this work.

Here, we propose a paradigm for studying non-Hermitian physics in cold Rydberg atomic gases, where the non-Hermitian term arises from dissipation induced by long-range Rydberg-Rydberg interactions. In contrast to other systems characterized by different types of interaction, such as those involving electron-electron and cavity-coupled interactions discussed in previous studies[19,53,54], our system features a different interaction and dissipation mechanisms. This leads to the unique non-Hermitian dynamics and provides a ideal platform for experimentally studying EPs. We observe a normal electro-magnetically induced transparency (EIT) spectrum under weak Rydberg atom interactions, whilst the peak of EIT splits into two when in strong interaction, indicating that the system crosses the second-order EPs. Additionally, our theoretical model confirms the existence of the third-order EP. In this scenario, the interaction is a dominant resource for system to produce non-Hermitian features, leading to rich hysteresis trajectories by varying probe intensities. The area of hysteresis loops reveals energy loss due to non-Hermiticity, and the dynamics can be tuned in various time scales.

RESULTS

Physical model

Our model is based on a three-level Rydberg atom system, as depicted in Fig. 1a. There are three atomic state manifolds of ground state $|g\rangle$, metastable state $|e\rangle$, and Rydberg state $|r\rangle$. The probe field with Rabi frequency (detuning) Ω_p (Δ_p) drives the transition $|g\rangle \leftrightarrow |e\rangle$, and the coupling field with Rabi frequency (detuning) Ω_c (Δ_c) drives the transition $|e\rangle \leftrightarrow |r\rangle$. The spontaneous decay rates of the states $|e\rangle$ and $|r\rangle$ are Γ_1 and γ, and γ_{eff} is the decay rate caused by Rydberg many-body interactions. A pair of atoms i and j at positions r_i and r_j excited to the Rydberg states $|r\rangle$ interact with each other via a van der Waals (vdW) potential $V_{vdW} \propto C_6/R^6$, where C_6 is the coefficient and R represents the distance between the Rydberg atoms.

By the EIT theory of the ensemble of cold atoms, long-range interactions between atoms limit the medium to behave as a collection of superatoms (Rydberg polaritons), each containing a blockade volume that can hold at most one Rydberg excitation as shown in Fig. 1b. The experimental setup is depicted by Fig. 1b, and the scan of

Ω_p^2 probes the dynamics of system response, as given in Fig. 1c. Here, the error bars are derived from the standard deviation calculated using three independent measurements, following the same estimation method used throughout the manuscript. The Rydberg polaritons display a dephasing feature when considering the interactions with each other, where the non-uniform distribution of the Rydberg atoms inside the polariton causes the position-dependent phase shifts[55,56].

The interaction between polaritons accelerates the decay of Rydberg atoms and causes a broadening of the Rydberg energy levels. This creates an additional dissipation channel for the Rydberg state $|r\rangle$ to its surrounding environment; further analysis can be found in the Methods section. In the rotating frame, the Hamiltonian of our system takes the form

$$H_1 = \begin{pmatrix} 0 & \Omega_p/2 & 0 \\ \Omega_p/2 & \Delta_p & \Omega_c/2 \\ 0 & \Omega_c/2 & \Delta_c + \Delta_p - i\gamma_{eff}/2 \end{pmatrix}, \quad (1)$$

where $\gamma_{eff} = V\rho_{rr}$ donates the effective non-Hermitian term. In our theoretical model, V represents the interaction strength and ρ_{rr} represents the population of the Rydberg atoms, with both factors contributing to the overall decay rate of Rydberg atoms. Obviously, when $\Delta_p = \Delta_c = 0$, this system is protected by CP-symmetry, and the non-Hermitian Hamiltonian satisfies $U_{CP}H_1 U_{CP}^{-1} = -H_1^*$ with $U_{CP} = \text{diag}(1, -1, 1)$[14].

The eigenvalues of H_1 are calculated as $E = E_1, E_2, E_3$. In this case, we can observe the Riemann surface showing real and imaginary parts of the eigenvalues of Hamiltonian H_1 [see more details in the Methods section]. The non-zero γ_{eff} induces imaginary parts of eigenvalues and generates the non-Hermitian features. By increasing γ_{eff}, the coalesce of three eigenvalues emerges and results in complex singularities in energy spectrum, we called these points as EPs[2,14].

Additionally, we reveal the existence of the third-order EP in our theoretical simulations, which shows promising potential for the application of precision measurement due to their enhanced sensitivity to perturbations[23,27]. At the third-order EPs, the real and imaginary parts of the eigenvalues exhibit a triple degeneracy. The three eigenvalues coalesce at a single point in both their real and imaginary components [see more details in the Methods section]. This unique
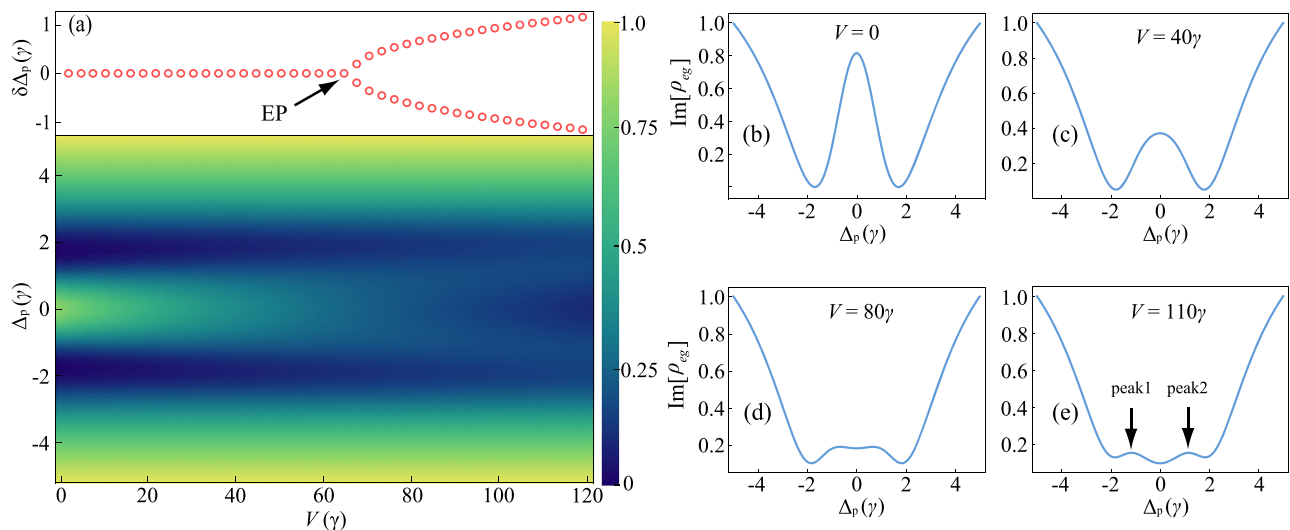
Fig. 2 | Theoretical phase diagram. a Theoretical spectrum Im[ρ_{eg}] versus the interaction strength V and detuning Δ_p. As the interaction strength gradually increases, Im[ρ_{eg}] decreases, as shown in (**b**) and (**c**). With further increase in interaction strength, the system transits an EP (marked by the black arrow in the up panel of (**a**)) and two distinct transmission peaks emerge [marked by the two black arrows] in the spectrum, as depicted in (**d**) and (**e**). The frequency difference $\delta\Delta_p$ between these emergent two peaks is indicated by the red circles in the up panel in (**a**). A value of 0 means that the system does not exhibit two distinguishable peaks. In these simulations, we set $\Gamma_1 = 6\gamma$, $\Delta_c = 0$, $\Omega_c = 3\gamma$, and $\Omega_p = \gamma$.

degeneracy at the third-order EPs is different from the case at the second-order EPs in PT symmetry two-level system where the real and imaginary parts of the eigenvalues will degenerate simultaneously[2,12,57].

The system also exhibits two second-order EPs, with a stable regime existing between these EPs [see more details in the Methods section]. In the scenario of the stable regime, a triple degeneracy of the eigenenergy exists in real space (Re[E_i] = 0, $i \in \{1, 2, 3\}$), while the corresponding imaginary parts separate into three distinct values. The eigenvalues satisfied $E_1 \neq E_2 \neq E_3$ and $E_i \in i\mathbb{R}$, indicating CP-symmetry breaking[14]. Outside this regime, when the eigenvalues of real space are completely non-degenerate, the eigenvalues of imaginary space separate into two values where two of the three are degenerate. Here, $E_1 = -E_2^*$ and $E_3 \in i\mathbb{R}$ [or $E_1 = -E_3^*$ and $E_2 \in i\mathbb{R}$], indicating the preservation of CP-symmetry.

We calculate the solution of master equation $\dot{\rho} = -i[\hat{H}_1, \rho] + \mathcal{L}[\rho]$ at the steady-state condition $\dot{\rho} = 0$. By the treatment of mean-field method, we map the spectrum of the normalized Im[ρ_{eg}] [corresponding to the transmission of EIT] versus the interaction strength V and detuning Δ_p, as shown by the down panel in Fig. 2a. With increase of V, for example, from $V = 0$ to $V = 110\gamma$, the peak of Im[ρ_{eg}] decreases and the neighbor two peaks emerge, as shown in Fig. 2b–e and the up panel in Fig. 2a. In this process, the system crosses the EPs, and the peak of Im[ρ_{eg}] splits into two, indicating that the degeneracy of one complex eigenvalue of system has been de-degenerated.

Non-Hermitian spectrum and exceptional point
The presence of strong interactions between Rydberg atoms leads to additional dissipation, which provides a platform to study non-Hermitian spectrum. In the experiment, we excite the ground state of a cold ensemble of ^{85}Rb atoms to Rydberg state $|47D_{5/2}, F = 5, m_F = -5\rangle$ by the EIT method, see more detailed information in Methods section. We measure the spectra by scanning probe detuning Δ_p from $\Delta_p = -2\pi \times 15$ MHz to $\Delta_p = 2\pi \times 15$ MHz under different probe intensities $(\Omega_p/2\pi)^2$.

As the probe intensity increases, the interaction between Rydberg atoms become progressively stronger. This enhanced interaction is similar to the effect of raising the interaction strength V in theoretical model, where both scenarios lead to an increase in the decay rate of Rydberg atoms due to enhanced interaction-induced dissipation [see more detail in Methods section]. By this way, we can map a phase diagram of system that responds to parameters of probe detuning Δ_p and intensity $(\Omega_p/2\pi)^2$. From $(\Omega_p/2\pi)^2 = 9$ MHz^2 to $(\Omega_p/2\pi)^2 = 64$ MHz^2, the dynamics of response are obtained. When the probe intensity $(\Omega_p/2\pi)^2$ is small [for example, $(\Omega_p/2\pi)^2 \leq 14.5$ MHz^2], the EIT spectrum is normal as the interaction between Rydberg atoms is weak. In this process, the system has three eigenvalues as we can see only one peak and two dips in Fig. 3b [the peak and dips result from one zero energy and two symmetric eigenenergy as described in ref. 58], and this corresponds to the regime of Hermiticity approximately [as the interaction is ignored].

When the probe intensity $(\Omega_p/2\pi)^2$ is large [for example, $(\Omega_p/2\pi)^2 > 14.5$ MHz^2], non-Hermiticity of system begins to emerge and the peak intensity of the EIT spectrum becomes weak, as shown in Fig. 3c. With a further increase of $(\Omega_p/2\pi)^2$, the peak of EIT spectrum splits into two peaks and the system undergoes the second-order EP [see the results in Fig. 3d, e]. At EP $((\Omega_p/2\pi)^2 = 36.5$ MHz$^2)$, a sudden change in the physical parameters breaks symmetry of system, leading to a bifurcation where the real and imaginary parts of system eigenvalue coalesce and split respectively. In this scenario, the presence of spectrum splitting post-EPs signatures the breaking of CP-symmetry[14]. The peaks in Fig. 3e are asymmetric due to the small shift on Rydberg energy level.

Hysteresis trajectories
The dependence on the transmission on the probe intensity allows us to observe hysteresis trajectories, which reflects the interplay between Rydberg atoms' response and theirs interaction. For all hysteresis trajectories measurements, the detuning values for both the coupling and probe beams were set to zero, which is consist with the conditions used in the theoretical calculations presented in the Methods section. Notably, all hysteresis trajectories measurements were conducted under weaker interaction strengths compared to the experimental conditions for observing EPs in Fig. 3, which required higher optical density. Hence, even at larger values of Ω_p^2, the system remained below the EPs during these measurements. Our investigation of hysteresis trajectories reveals the non-Hermitian characteristics of the Rydberg atom system, highlighting the dynamic behavior below the EPs and the emergence of hysteresis loops.
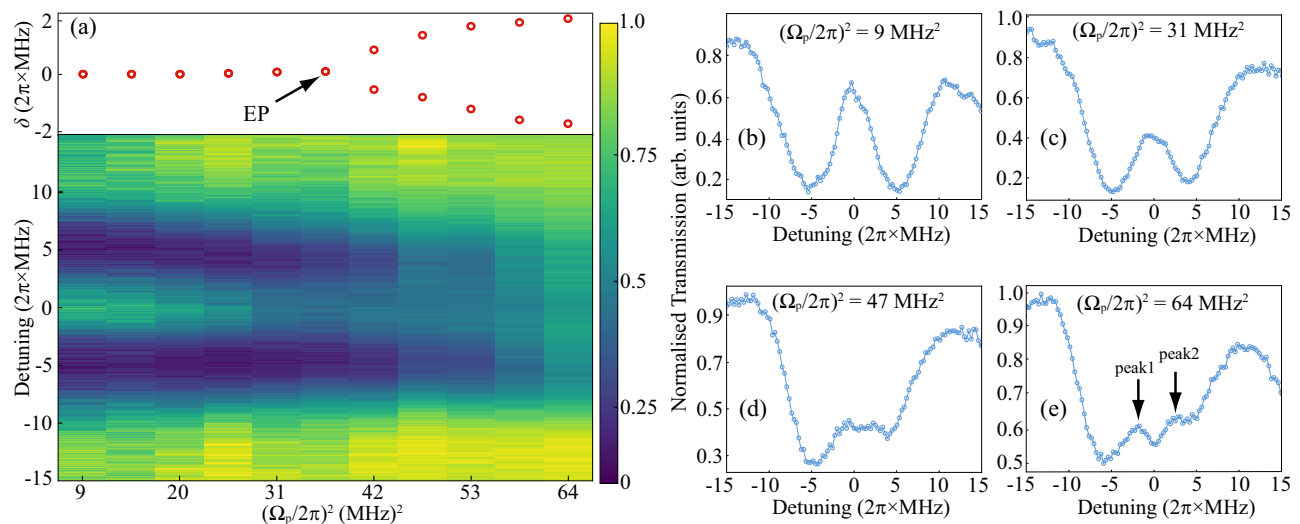
Fig. 3 | Measured phase diagram. a Measured EIT transmission spectrum versus the probe intensity, which is proportional to Ω_p^2. The EIT spectrum shows a visible transmission peak when the probe intensity is low, which means that the interaction between Rydberg atoms are so weak that the system maintains Hermiticity, as shown in (**b**). As the probe intensity grows, non-Hermiticity of the Rydberg atoms system begins to emerge, which is manifested in the transmission spectrum as a weakening of the transmission intensity, as shown in (**c**). And as the probe intensity continues to increase, the strong interaction between the Rydberg atoms brings out the eigenenergy bifurcation, and two transmission peaks appear in the EIT spectrum, as shown in (**d**) and (**e**). The red circles in the upper panel of (**a**) indicate the frequency shifts δ of the two transmission peaks.

By scanning $(\Omega_p/2\pi)^2$ from 0 MHz^2 to 140.6 MHz^2 and vice versus, we can obtain a series of closed circles under different optical densities (ODs), as shown in Fig. 4a–d. In the regime with small atoms numbers (which corresponds to large atomic distance R), we can find that the invariance of the linearity of transmission to probe intensity. This implies the interaction-induced dissipation does not dominate by comparing the inherent decay rate γ of Rydberg state, corresponding to the physical process under the regime of Hermiticity, as given by the case of OD = 4.6 in Fig. 4a. When we increase OD, for example, from OD = 6.8 to OD = 8.9, the transmission for positive and negative scans undergoes behavior with different scaling. The physics behind this phenomenon is non-Hermiticity: at larger OD, the Rydberg atomic interaction-induced dissipation cannot be ignored and the response is no longer linear to probe intensity and results in the emergence of hysteresis loop, see the area between pink and blue data given in Fig. 4b–d.

We also model the trajectories of system using the Lindblad master equation $\dot{\rho} = -i[\hat{H}_1, \rho] + \mathcal{L}[\rho]$, where the operator $\mathcal{L}$ describes the decay rate of system. The theoretical results predict the hysteresis loops of $\mathrm{Im}[\rho_{eg}]$, see more details in Methods section. The phenomenon of hysteresis loop is counter-intuitive because the transmission does not overlap under the same probe intensity, in which the current state of system not only depends on its current inputs but also on its past states and inputs. The increase of atoms number through probe intensity forms structured Rydberg clusters by near neighbor interaction, the induced dissipation makes the clusters' behaviour different from the case of few atoms. If the probe intensity is then reduced conversely, the atoms retains some level of dissipation. To completely release the dissipation of atoms, only small reduction of probe intensity is required in the reversal scanning, see more detailed information in Methods section. This asymmetry in the response of the Rydberg atoms to increasing and decreasing probe intensity is a clear manifestation of hysteresis.

The direction of hysteresis trajectories is reversal to magnetic hysteresis in ferromagnetic material[59], but same with the normal elastic hysteresis of rubber[60]. The different directions of trajectories result from the distinct physical mechanism behind these hysteresis. In our experiment, different ODs (which relate to different numbers of atoms and interaction strengths) can alter how the system responds to changes in probe intensity, and influences the size (area) and shape of the hysteresis loop observed experimentally, as illustrated in Fig. 4a–d. In terms of energy, the area enclosed by the hysteresis loop quantifies the energy loss during scanning $(\Omega_p/2\pi)^2$.

The hysteresis loop also depends on the coupling Rabi frequency Ω_c, as given in Fig. 4e–h. We can find that the hysteresis loop only appears within a range of Ω_c. When we use a relative small Rabi frequency of $\Omega_c = 2\pi \times 13.3$ MHz, the corresponding excited Rydberg atoms number cannot provide enough interaction strength between atoms, thus resulting in normal trajectories shown in Fig. 4e. When we set $\Omega_c = 2\pi \times 27.8$ MHz, the interaction-induced dissipation affects the scaling of transmission to probe intensity, then generates a hysteresis loop given in Fig. 4f. If the system is driven under a large Ω_c (for example, $\Omega_c = 2\pi \times 38.6$ MHz and $\Omega_c = 2\pi \times 45.6$ MHz) that the atoms have no time to respond, then the hysteresis loop shrinks and disappears.

Furthermore, we also investigated the effect of the principal quantum number n on the hysteresis loop while keeping OD and Ω_c constant, which maintained an equal number of excited atoms, as shown in Fig. 4i–l. In Rydberg atom system, changes in the principal quantum number n directly influence the value of C_6, thereby influencing the interaction strength $V \propto C_6$. At relatively low values of n [such as $n = 40$], the interactions between Rydberg atoms are weak, resulting in less energy dissipation. This leads to a smaller hysteresis loop in the EIT spectrum, as illustrated in Fig. 4i. As the principal quantum number increases, the interaction strength correspondingly intensifies, leading to greater energy dissipation within the system. This enhanced dissipation manifests as an expansion of the hysteresis loop, which further reveals the mechanism of interaction-induced dissipation in our system, as illustrated in Fig. 4j–l.

Hysteresis loops dynamics

The underlying mechanism behind the physical system is based on interaction-induced dissipation, which exhibits how quickly the system respond to changes in probe field. This enables us to capture the time-dependent behavior of system as it undergoes changes in external conditions. In the experiment, we record hysteresis loops versus the
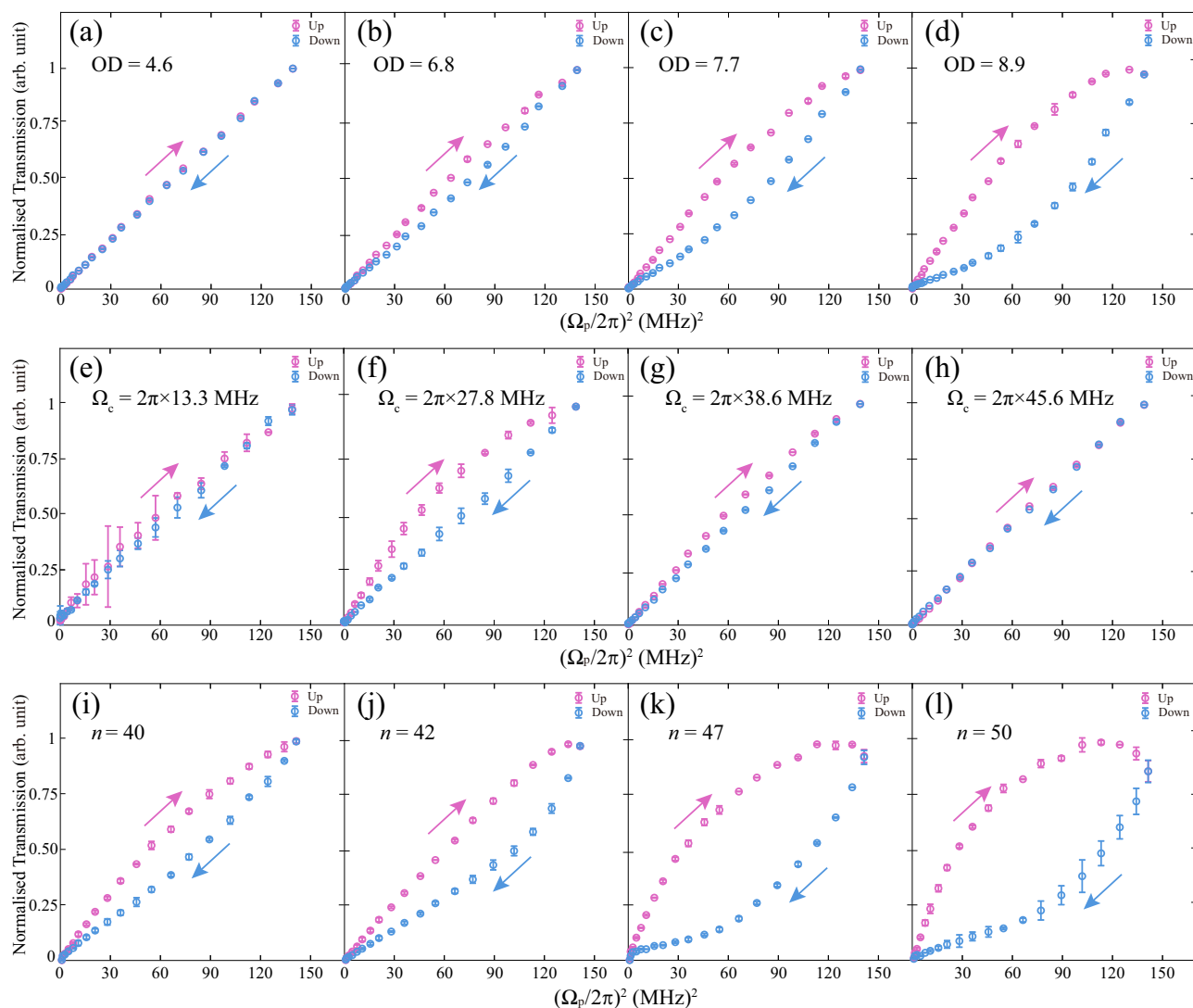
Fig. 4 | Measured hysteresis trajectories versus OD, Ω_c, and n. a–d Measured transmission with scanning Ω_p^2 in positive (pink, up) and negative (blue, down) directions under optical densities of OD = 4.6 (**a**), OD = 6.8 (**b**), OD = 7.7 (**c**) and OD = 8.9 (**d**). The pink circle data represents the transmission when increasing $(\Omega_p/2\pi)^2$ from 0 MHz^2 to 140.6 MHz^2, and the blue circle data shows the transmission by scanning $(\Omega_p/2\pi)^2$ from 140.6 MHz^2 to 0 MHz^2 with the same sweep rate. **e**, **f** Measured transmission versus the coupling field's Rabi frequency of $\Omega_c = 2\pi \times 13.3$ MHz (**e**), $\Omega_c = 2\pi \times 27.8$ MHz (**f**), $\Omega_c = 2\pi \times 38.6$ MHz (**g**) and $\Omega_c = 2\pi \times 45.6$ MHz (**h**). **i–l** Measured transmission versus the principal quantum number of $n = 40$ (**i**), $n = 42$ (**j**), $n = 47$ (**k**), $n = 50$ (**l**).

scanning time T_s and measure the area enclosed by hysteresis loop. The results are found in Fig. 5a. In this scenario, we consider two cases of OD = 8.0 (blue data in Fig. 5a) and OD = 4.5 (red data in Fig. 5a) and show the difference between them. We fit the measured areas using dashed lines, where the fit function is $y = ae^{-b(x-d)^\alpha} + c$ ($a = -64.9$, $b = 0.053$, $c = 65.3$, $d = 5$, $\alpha = 1.5$) for OD = 8.0 and the fit function is $y = 0$ for OD = 4.5. For OD = 4.5, the atoms are dilute, the linearity of transmission on $(\Omega_p/2\pi)^2$ is invariant to the scanning time T_s as the interaction is ignored. However, when we increase OD to 8.0, hysteresis loops appear and the area grows versus T_s.

In our experiment, a fast scan accumulates a small number of Rydberg atoms within limited time interval to each data, which makes the interactions so weak that the effect from non-Hermiticity might not dominate, see the results shown in Fig. 5b. As T_s increases, this corresponds to more excited Rydberg atoms for a relatively large time interval and interactions between the Rydberg atoms cannot be ignored, thus the effect of non-Hermiticity emerges, as illustrated in Fig. 5c. For our experiment, there's a characteristic measurement time of $T_s \sim 5\,\mu s$, where shorter scan times capture system's transient behavior, while longer scan times converge to the equilibrium value.

The results in Fig. 5d, e show examples of small OD, the variance of scanning time do not affect the linearity of transmission to probe intensity.

DISCUSSION

Our experiment serves as a preliminary verification test for non-Hermitian many-body physics[1,61], and promotes the applications towards studying high-order EPs and symmetry breaking in high-dimension systems. For example, according to ref. 14, both sides of third-order EPs have different signs of winding number, thus providing a platform to study the topological properties (such as topology stability, topological phase transition) around EPs in the Rydberg system. In addition, the phenomenon of hysteresis loops enables us to build an interface between hysteresis dynamics and non-Hermitian physics, this could provide an experimental correspondence to theory[62].

In summary, we have observed interaction-induced second-order EPs and hysteresis loops in a cold Rydberg atomic gas. The interaction between Rydberg atoms endows system a dissipation channel, leading to non-Hermitian many-body dynamics. In the experiment, we observe interaction-induced hysteresis loops, in which the dynamics of the
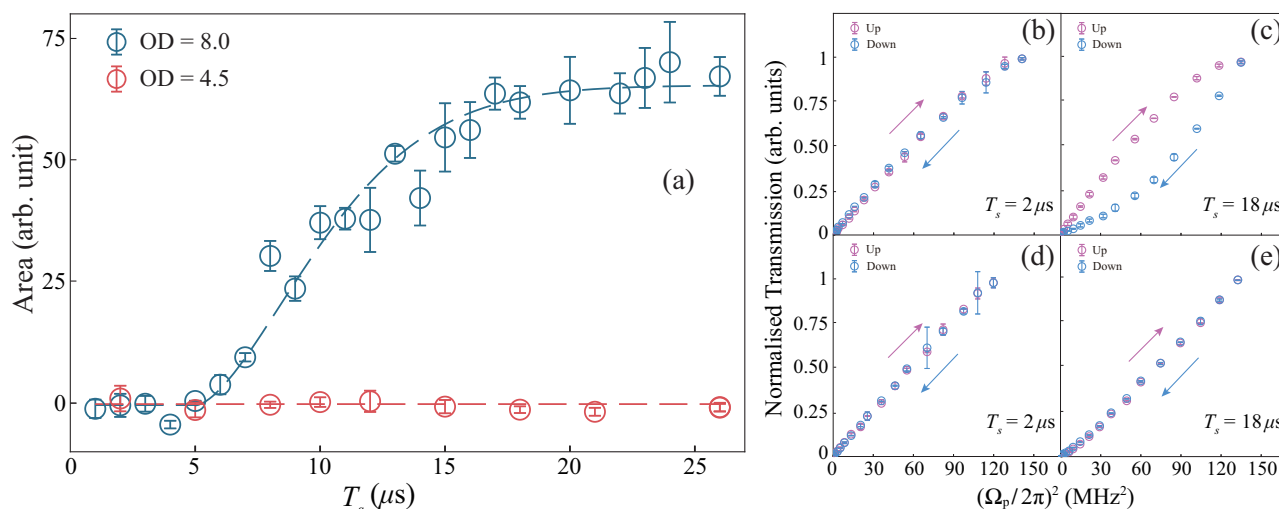
Fig. 5 | Hysteresis dynamics. a The measured area of hysteresis loops versus the scan time T_s under OD = 8 (blue circles) and OD = 4.5 (red circles). The blue data is fit by the function of $y = ae^{-b(x-d)^\alpha} + c$ ($a = -64.9, b = 0.053, c = 65.3, d = 5, \alpha = 1.5$), and the red data is fit by the function of $y = 0$. **b**, **c** are the measured transmission (OD = 8) in positive and negative scanning $(\Omega_p/2\pi)^2$ by setting $T_s = 2\,\mu$s and $T_s = 18\,\mu$s, respectively. **d**, **e** are the measured transmission (OD = 4.5) in positive and negative scanning $(\Omega_p/2\pi)^2$ by setting $T_s = 2\,\mu$s and $T_s = 18\,\mu$s, respectively.

system is dramatically distinct by comparing with weak-interaction case. In the context of a cold Rydberg atomic gas, the emergence of EPs and the hysteresis loops due to many-body interactions help us to explore the rich dynamics between many-body interaction and the non-Hermitian physics.

Methods
Details of the experimental setup
To study non-Hermitian many-body dynamics, the emergence of EPs, and hysteresis trajectories, we prepare a cold ensemble of ^{85}Rb atoms trapped in a three-dimensional magneto-optic trap (MOT). The atomic ensemble is prepared in the ground state $|g\rangle = |5S_{1/2}, F = 3, m_F = -3\rangle$ by an optical pumping process. In experiment, we wrapped the MOT with a double-layer magnetic shield system. By this way, we can shield the system from external magnetic fields, and it can reduce the internal magnetic field to less than 10 mGauss. A guiding magnetic field is generated by a pair of Helmholtz coils symmetrically placed around the atomic ensemble, and the direction of the field is along the direction of beams propagation. By this way, the direction of the quantisation axis of the system is confirmed.

We used a two-photon transition scheme to excite ^{85}Rb atoms from the ground state to the Rydberg state. The probe beam ($\omega_p \approx 10\,\mu$m) driving the atoms from the ground state $|g\rangle$ to the intermediate excited state $|e\rangle = |5P_{3/2}, F = 4, m_F = -4\rangle$, and the coupling beam ($\omega_c \approx 20\,\mu$m) then drives the transition from $|e\rangle$ to the Rydberg state $|r\rangle = |47D_{5/2}, F = 5, m_F = -5\rangle$, as shown in Fig. 1a in the main text. The probe beam and coupling beam are focused into the cold atomic ensemble, and we used the Pound-Drever-Hall method to lock probe and coupling beams frequency, thus constituting the EIT process. We use a beam splitter to split the coupled beam into two beams before focusing into the cold atomic ensemble, and the intensity of one of these beams was detected using a photodetector. This method allows us to monitor the intensity of the coupling beam in real time. The transmission signals are detected using a photo-multiplier tube.

In experiment, we loaded a triangular wave signal that was generated using a signal generator (RIGOL DG4102) onto the acousto-optic modulator. By this way, we produce the process of increasing beam intensity (Up process) and intensity reduction process (Down process). To better compare the Up and Down

processes, we perform an inversion of the Down process, as shown in Fig. 1c in the main text.

Non-Hermitian Hamiltonian
The system of interest is schematically depicted in Fig. 1b, where two optical fields with spatial overlap comprise a counter-collinear weak-probe field and a strong-control field. The Rydberg atomic level structure is the three-level EIT configuration shown in Fig. 1a. The strong-control field with the Rabi frequency (Ω_c) and detuning (Δ_c) drives the transition $|e\rangle \leftrightarrow |r\rangle$; the weak-probe field with the Rabi frequency (Ω_p) and detuning (Δ_p) drives the transition $|g\rangle \leftrightarrow |e\rangle$, and the two-photon detuning between two counter-collinear fields is $\Delta = \Delta_p - \Delta_c$. Under the Rydberg EIT configurations, the population is mainly distributed in $|g\rangle$. The spontaneous decay of the state $|e\rangle$ ($|r\rangle$) at a rate Γ_1 (γ). The interactions between excited Rydberg atoms are reflected in the optical responses of atoms and the transmission of the probe field.

The Hamiltonian in the interaction picture and rotating-wave approximation reads ($\hbar = 1$),

$$H_{many} = \sum_{j=1}^{N}\left[-(\Delta_p + \Delta_c)\hat{\sigma}_{rr}^j - \left(\Omega_p\sigma_{eg}^j + \Omega_c\sigma_{re}^j + \text{H.c.}\right)\right]$$
$$+ \sum_{j=1}^{N}\left[-\Delta_p\hat{\sigma}_{ee}^j + \sum_{j<k}V_{jk}\sigma_{rr}^j\sigma_{rr}^k\right], \quad (2)$$

where $\sigma_{\alpha\beta}^j = |\alpha_j\rangle\langle\beta_j|$ ($\alpha, \beta = e, g, r$). We then consider the mean-field approximation, in which a single atom is immersed in a field generated by the interactions between itself and other atoms. Consequently, the problem of solving the dynamic many-body system is reduced to addressing the dynamics of one single atom within that field, treating the other atoms as part of the environment. The Hamiltonian can be written as

$$H_{many} = H_1 \otimes I_{N-1} + I_1 \otimes H_{N-1} + H_I, \quad (3)$$

where H_I describes the interaction between the single atom and the environment, H_1 is the single atom Hamiltonian, H_{N-1} is the Hamiltonian of the environment, and I_1 (I_{N-1}) denotes the identity in the Hilbert space H_1 (H_{N-1}). Consider the two-body interaction between the Rydberg atoms, the interaction distance R_j represents the single atom
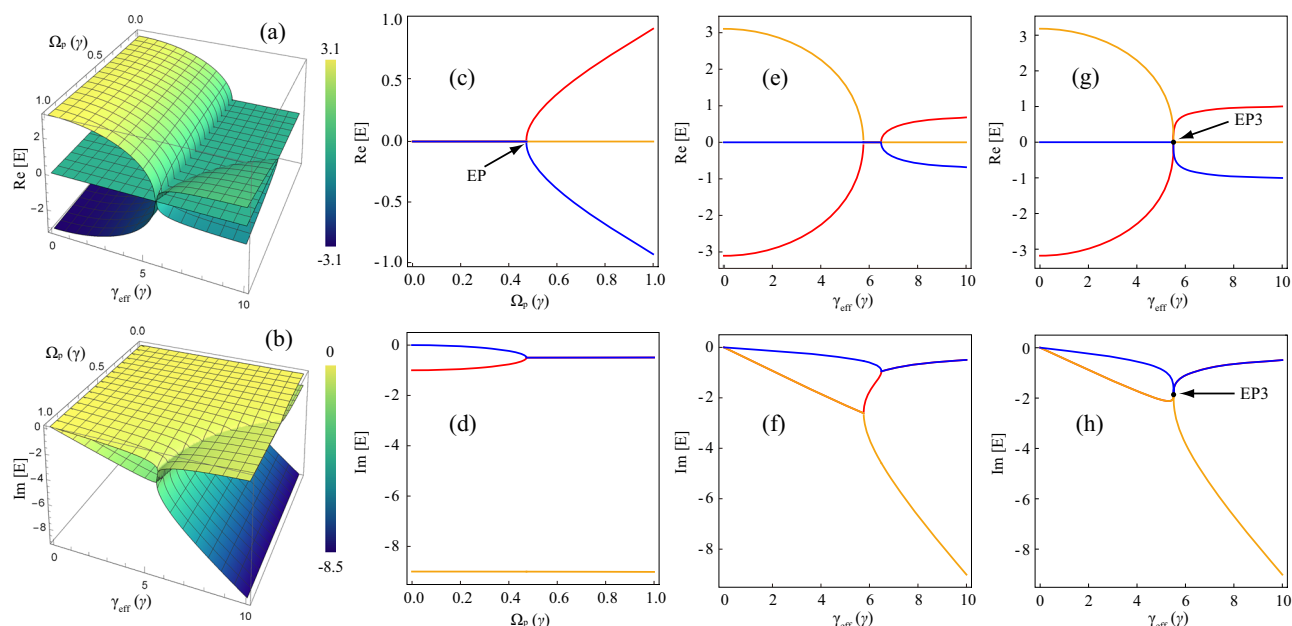
Fig. 6 | Theoretical simulations of third-order EPs. a Real and **b** imaginary parts of the system eigenvalues as a function of Ω_p and γ_{eff}. In these simulations, we set $\Delta_c = \Delta_p = 0$, $\Omega_c = 3\gamma$. **c**, **d** are the real and imaginary parts of the system eigenvalues as a function of Ω_p with $\gamma_{eff} = 10\gamma$. **e**, **f** represent the system eigenvalues as a function of γ_{eff} with $\Omega_p = 0.8\gamma$. **g**, **h** represent the system eigenvalues as a function of γ_{eff} with $\Omega_p = 1.061\gamma$. The black dots represent the third-order EP of the system. The red, orange, and blue lines correspond to the values of E_1, E_2, and E_3, respectively.

between the atom in the environment. Then the total Rydberg state $|r_N\rangle = \sum_{j=1}^{N-1} |r_1\rangle \otimes |r_j\rangle$ evolves according to

$$\hat{U}(t) = \sum_{j=1}^{N-1} e^{-iV_j t} \left(|r_1\rangle \otimes \sum_{i=1}^{N-1} |r_i\rangle_j \right) \left(\langle r_1| \otimes \sum_{i=1}^{N-1} \langle r_i|_j \right). \quad (4)$$

Since the distance between the single atom and the j-atom in the environment R_j is different, in regarding the energy shifts on $|r_1\rangle$, it is necessary to consider the distinct contributions from the j-atom. The atom far away in the environment produces a small shift, otherwise the shift will be large, due to the form of van der Waals (vdW) potential $V_{vdW} \propto C_6/R^6$. Overall, this effect is to widen the energy level $|r_1\rangle$ with an effective width γ_{eff}. Here, we consider the reduced density matrix of the single-atom system, and the non-Hermitian Hamiltonian has the form

$$H_1 = -\Delta_p \hat{\sigma}_{ee} - \left(\Delta_p + \Delta_c - \frac{i\gamma_{eff}}{2}\right)\hat{\sigma}_{rr} \\ - \left(\Omega_p \sigma_{eg} + \Omega_c \sigma_{re} + \text{H.c.}\right), \quad (5)$$

where γ_{eff} reveals the effective decay rate induced by the interaction of the environment. The eigenvalues of H_1 are given by

$$E_1 = \frac{1}{6}\left(\frac{C}{\sqrt[3]{B+iA}} - \sqrt[3]{4B+4iA} - 2i\gamma_{eff}\right), \quad (6)$$

$$E_2 = \frac{1}{12}\left((1-i\sqrt{3})\sqrt[3]{4B+4iA} - \frac{(1+i\sqrt{3})C}{\sqrt[3]{B+iA}} - 4i\gamma_{eff}\right), \quad (7)$$

$$E_3 = \frac{1}{12}\left((1+i\sqrt{3})\sqrt[3]{4B+4iA} - \frac{(1-i\sqrt{3})C}{\sqrt[3]{B+iA}} - 4i\gamma_{eff}\right), \quad (8)$$

where

$$A = 9\gamma_{eff}\left(\Omega_c^2 - 2\Omega_p^2\right) - 2\gamma_{eff}^3, \quad (9)$$

$$B = 3\sqrt{3}\sqrt[3]{\gamma_{eff}^2\left(\Omega_c^4 + 20\Omega_c^2\Omega_p^2 - 8\Omega_p^4\right) - 4\Omega_p^2\gamma_{eff}^4 - 4\left(\Omega_c^2 + \Omega_p^2\right)^3}, \quad (10)$$

$$C = 2\sqrt[3]{2}\left(\gamma_{eff}^2 - 3\left(\Omega_c^2 + \Omega_p^2\right)\right). \quad (11)$$

By setting the parameters $\Omega_c = 3\gamma$ and $\Delta_p = \Delta_c = 0$, we obtain the real and imaginary parts of the system eigenvalues as a function of γ_{eff} and Ω_p, as given in Fig. 6.

From these results, for example in Fig. 6c, d, we can find that the second-order EPs appear. Before the EPs, the real parts of the three eigenvalues coalesce and the imaginary parts of the eigenvalues split, characterized by $E_1 \neq E_2 \neq E_3$ and $E_i \in i\mathbb{R}$, indicating CP-symmetry breaking. In contrast, after the EPs, the eigenvalues satisfy $E_1 = -E_2^*$ and $E_3 \in i\mathbb{R}$ [or $E_1 = -E_3^*$ and $E_2 \in i\mathbb{R}$], thereby preserving CP-symmetry[14]. In addition, when $\Omega_p = 0.8\gamma$, a second-order EPs first appear, and retain stable in a range of $5.77\gamma < \gamma_{eff} < 6.49\gamma$ (in the stable region, CP-symmetry breaking occurs) and then enter another second-order EPs (outside the stable region, the system preserves CP-symmetry), as shown in Fig. 6e, f. When $\Omega_p = 1.061\gamma$, the third-order EP appear, where both the real and imaginary parts of the system exhibit a triple degeneracy, and the system always preserving CP-symmetry, as shown in Fig. 6g, h.

Lindblad master equation

In the mean-field treatment, we solve the Lindblad master equation by adding the dissipation term $\Gamma_2 \rightarrow \gamma + \gamma_{eff} = \gamma + V\rho_{rr}$[42,55,56,63–66], and obtain

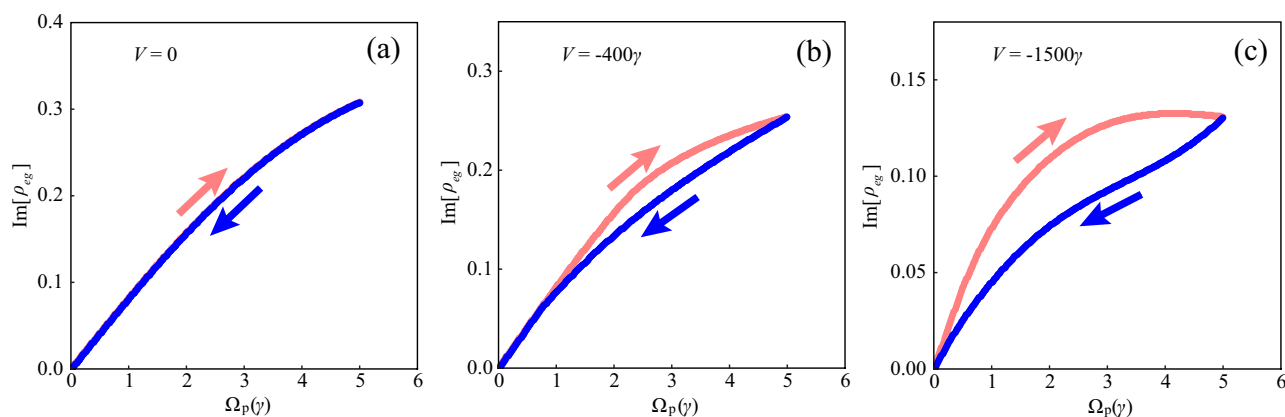**Fig. 7 | Hysteresis trajectories of Im[ρ_{eg}] versus interaction strength *V*.** The simulated hysteresis versus interaction strength are given in (**a**) $V = 0$, (**b**) $V = -400\,\gamma$, and (**c**) $V = -1500\,\gamma$. The pink and blue arrows represents the positive and negative scanning Ω_p. In these simulations, we set $\Gamma_1 = 12\gamma$, $\Delta_c = \Delta_p = 0$, $\Omega_c = 0.25\gamma$, and $\rho_{re}(t = 0) = 0.1$.

the following equations:

$$\dot{\rho}_{gg} = i\frac{\Omega_p}{2}(\rho_{eg} - \rho_{ge}) + \Gamma_1\rho_{ee}, \qquad (12)$$

$$\dot{\rho}_{ee} = i\frac{\Omega_p}{2}(\rho_{ge} - \rho_{eg}) + i\frac{\Omega_c}{2}(\rho_{re} - \rho_{er}) - \Gamma_1\rho_{ee} + \Gamma_2\rho_{rr}, \qquad (13)$$

$$\dot{\rho}_{rr} = i\frac{\Omega_c}{2}(\rho_{er} - \rho_{re}) - \Gamma_2\rho_{rr}, \qquad (14)$$

$$\dot{\rho}_{re} = i\frac{\Omega_c}{2}(\rho_{ee} - \rho_{rr}) - i\frac{\Omega_p}{2}\rho_{rg} - \left(i\Delta_c + \frac{\Gamma_2}{2} + \frac{\Gamma_1}{2}\right)\rho_{re}, \qquad (15)$$

$$\dot{\rho}_{er} = i\frac{\Omega_c}{2}(\rho_{rr} - \rho_{ee}) + i\frac{\Omega_p}{2}\rho_{gr} + \left(i\Delta_c - \frac{\Gamma_2}{2} - \frac{\Gamma_1}{2}\right)\rho_{er}, \qquad (16)$$

$$\dot{\rho}_{rg} = i\frac{\Omega_c}{2}\rho_{eg} - i\frac{\Omega_p}{2}\rho_{re} - \left(i(\Delta_p + \Delta_c) + \frac{\Gamma_2}{2}\right)\rho_{rg}, \qquad (17)$$

$$\dot{\rho}_{gr} = i\frac{\Omega_p}{2}\rho_{er} - i\frac{\Omega_c}{2}\rho_{ge} + \left(i(\Delta_p + \Delta_c) - \frac{\Gamma_2}{2}\right)\rho_{gr}, \qquad (18)$$

$$\dot{\rho}_{eg} = i\frac{\Omega_p}{2}(\rho_{gg} - \rho_{ee}) + i\frac{\Omega_c}{2}\rho_{rg} - \left(i\Delta_p + \frac{\Gamma_1}{2}\right)\rho_{eg}, \qquad (19)$$

$$\dot{\rho}_{ge} = i\frac{\Omega_p}{2}(\rho_{ee} - \rho_{gg}) - i\frac{\Omega_c}{2}\rho_{gr} + \left(i\Delta_p - \frac{\Gamma_1}{2}\right)\rho_{ge}. \qquad (20)$$

First, we consider the case of no-interaction ($\gamma_{eff} = 0$) and calculate the steady-state solution ($\dot{\rho}_{ij} = 0$, where i, j represent the states of $|g\rangle$, $|e\rangle$, and $|r\rangle$), we therefore obtained the element of density matrices ρ_{eg} and ρ_{rr} versus Δ_p and Γ_2, with forms of $\rho_{eg}(\Delta_p, \gamma)$ and $\rho_{rr}(\Delta_p, \gamma)$, respectively. Then, by considering the interaction induced non-Hermiticity, we obtain the modified matrix element $\rho_{eg}(\Delta_p, \gamma + V\rho_{rr})$ with the mean-field approximation $\Gamma_2 \rightarrow \gamma + V\rho_{rr}$. We plot Im[$\rho_{eg}$] versus Δ_p and *V*, the phase diagram and transmission lines are given by Fig. 2. In this framework, we keep Rydberg atom population ρ_{rr} fixed, assuming it behaves as in a non-interacting scenario where it varies only with Δ_p. By adjusting interaction strength *V*, we can effectively control the decay rate of Rydberg state.

To simulate hysteresis trajectories, the state of atoms is influenced not only by the external input but also by their previous states.

In particular, the systematic evolution is dependent on the direction of scanning Ω_p. Thus, we replace the time-dependent population $\rho_{rr}(t)$ by the term $\dot{\rho}_{rr}(t)$ according to Eq. (14): $\dot{\rho}_{rr}(t) = i\Omega_c/2\Gamma_2(\rho_{er}(t) - \rho_{re}(t)) - \dot{\rho}_{rr}(t)/\Gamma_2$. Thus, the slope of Rydberg population $\dot{\rho}_{rr}(t)$ plays a crucial role in influencing the transient behavior of $\rho_{rr}(t)$.

In the simulations, we treat the results $\rho_{ij}(t)$ at time *t* as the initial conditions for calculating $\rho_{ij}(t + \Delta t)$ at time $t + \Delta t$. This approach effectively captures the inherent memory effects in the system's evolution. We specifically examined the time-dependent component Im[$\rho_{eg}(t)$] while scanning Ω_p both positively and negatively, across various interaction strengths: $V = 0$, $V = -400\gamma$, and $V = -1500\gamma$. The corresponding results are presented in Fig. 7a–c. These results reveal intriguing behaviors of the scanned trajectories. In the case with no interaction ($V = 0$, Fig. 7a), the trajectories exhibit a coincident pattern, indicating that the system's dynamics are symmetric. However, when considering interactions, specifically at $V = -400\gamma$ and $V = -1500\gamma$, as depicted in Fig. 7b, c, the trajectories form closed loops.

The emergence of these hysteresis loops underscores the critical role of interaction strength in shaping the dynamical properties of the system. Moreover, the observed dynamics align closely with experimental observations illustrated in Fig. 4a–l and Fig. 5a–e, which further corroborates the relevance of our simulation results. This consistency between theoretical predictions and experimental observations highlights the exact complex interplay between system memory and interaction, providing valuable insights into the underlying mechanisms governing the observed phenomena.

Data availability
The data generated in this study have been deposited in the Zenodo database (https://zenodo.org/records/14380778).

Code availability
The custom codes used to produce the results presented in this paper are available from the corresponding authors upon request.

References
1. Miri, M.-A. & Alu, A. Exceptional points in optics and photonics. *Science* **363**, eaar7709 (2019).
2. Mandal, I. & Bergholtz, E. J. Symmetry and higher-order exceptional points. *Phys. Rev. Lett.* **127**, 186601 (2021).
3. Wang, Y.-C., You, J.-S. & Jen, H.-H. A non-hermitian optical atomic mirror. *Nat. Commun.* **13**, 4598 (2022).
4. Ding, K., Fang, C. & Ma, G. Non-hermitian topology and exceptional-point geometries. *Nat. Rev. Phys.* **4**, 745 (2022).

5. Yoshida, T. & Hatsugai, Y. Fate of exceptional points under interactions: reduction of topological classifications. *Phys. Rev. B* **107**, 075118 (2023).

6. Wang, C. et al. Electromagnetically induced transparency at a chiral exceptional point. *Nat. Phys.* **16**, 334 (2020).

7. Shu, X. et al. Chiral transmission by an open evolution trajectory in a non-hermitian system. *Light Sci. Appl.* **13**, 65 (2024).

8. Huang, Y., Shen, Y., Min, C., Fan, S. & Veronis, G. Unidirectional reflectionless light propagation at exceptional points. *Nanophotonics* **6**, 977 (2017).

9. Du, C. X., Wang, G., Zhang, Y. & Wu, J. H. Light transfer transitions beyond higher-order exceptional points in parity-time and anti-parity-time symmetric waveguide arrays. *Opt. Express* **30**, 20088 (2022).

10. Ding, F., Deng, Y., Meng, C., Thrane, P. C. & Bozhevolnyi, S. I. Electrically tunable topological phase transition in non-hermitian optical mems metasurfaces. *Sci. Adv.* **10**, eadl4661 (2024).

11. Gong, J. & Lee, C. H. Topological phase transitions have never been faster. *Nat. Phys.* **20**, 12 (2024).

12. El-Ganainy, R. et al. Non-hermitian physics and PT symmetry. *Nat. Phys.* **14**, 11 (2018).

13. Li, A. et al. Exceptional points and non-hermitian photonics at the nanoscale. *Nat. Nanotechnol.* **18**, 706 (2023).

14. Delplace, P., Yoshida, T. & Hatsugai, Y. Symmetry-protected multifold exceptional points and their topological characterization. *Phys. Rev. Lett.* **127**, 186602 (2021).

15. Rosa, M. I., Mazzotti, M. & Ruzzene, M. Exceptional points and enhanced sensitivity in PT-symmetric continuous elastic media. *J. Mech. Phys. Solids.* **149**, 104325 (2021).

16. Yang, M., Zhu, L., Zhong, Q., El-Ganainy, R. & Chen, P.-Y. Spectral sensitivity near exceptional points as a resource for hardware encryption. *Nat. Commun.* **14**, 1145 (2023).

17. Peng, B. et al. Loss-induced suppression and revival of lasing. *Science* **346**, 328 (2014).

18. Hodaei, H., Miri, M. A., Heinrich, M., Christodoulides, D. N. & Khajavikhan, M. Parity-time–symmetric microring lasers. *Science* **346**, 975 (2014).

19. Dogra, N. et al. Dissipation-induced structural instability and chiral dynamics in a quantum gas. *Science* **366**, 1496 (2019).

20. Wang, K. et al. Experimental simulation of symmetry-protected higher-order exceptional points with single photons. *Sci. Adv.* **9**, eadi0732 (2023).

21. Chitsazi, M., Li, H., Ellis, F. & Kottos, T. Experimental realization of Floquet PT-symmetric systems. *Phys. Rev. Lett.* **119**, 093901 (2017).

22. Assawaworrarit, S., Yu, X. & Fan, S. Robust wireless power transfer using a nonlinear parity–time-symmetric circuit. *Nature* **546**, 387 (2017).

23. Chen, W., Kaya Özdemir, Ş., Zhao, G., Wiersig, J. & Yang, L. Exceptional points enhance sensing in an optical microcavity. *Nature* **548**, 192 (2017).

24. Lau, H. K. & Clerk, A. A. Fundamental limits and non-reciprocal approaches in non-hermitian quantum sensing. *Nat. Commun.* **9**, 4320 (2018).

25. Budich, J. C. & Bergholtz, E. J. Non-hermitian topological sensors. *Phys. Rev. Lett.* **125**, 180403 (2020).

26. Li, Z. et al. Synergetic positivity of loss and noise in nonlinear non-hermitian resonators. *Sci. Adv.* **9**, eadi0562 (2023).

27. Liang, C., Tang, Y., Xu, A.-N. & Liu, Y.-C. Observation of exceptional points in thermal atomic ensembles. *Phys. Rev. Lett.* **130**, 263601 (2023).

28. Hamazaki, R., Kawabata, K. & Ueda, M. Non-hermitian many-body localization. *Phys. Rev. Lett.* **123**, 090603 (2019).

29. Matsumoto, N., Kawabata, K., Ashida, Y., Furukawa, S. & Ueda, M. Continuous phase transition without gap closing in non-hermitian quantum many-body systems. *Phys. Rev. Lett.* **125**, 260601 (2020).

30. Kawabata, K., Shiozaki, K. & Ryu, S. Many-body topology of non-hermitian systems. *Phys. Rev. B* **105**, 165137 (2022).

31. Saffman, M., Walker, T. G. & Mølmer, K. Quantum information with Rydberg atoms. *Rev. Mod. Phys.* **82**, 2313 (2010).

32. Adams, C. S., Pritchard, J. D. & Shaffer, J. P. Rydberg atom quantum technologies. *J. Phys. B: At. Mol. Opt. Phys.* **53**, 012002 (2019).

33. Browaeys, A. & Lahaye, T. Many-body physics with individually controlled Rydberg atoms. *Nat. Phys.* **16**, 132 (2020).

34. Lee, T. E., Häffner, H. & Cross, M. C. Collective quantum jumps of Rydberg atoms. *Phys. Rev. Lett.* **108**, 023602 (2012).

35. Carr, C., Ritter, R., Wade, C., Adams, C. S. & Weatherill, K. J. Nonequilibrium phase transition in a dilute Rydberg ensemble. *Phys. Rev. Lett.* **111**, 113901 (2013).

36. Schempp, H. et al. Full counting statistics of laser excited Rydberg aggregates in a one-dimensional geometry. *Phys. Rev. Lett.* **112**, 013002 (2014).

37. Marcuzzi, M., Levi, E., Diehl, S., Garrahan, J. P. & Lesanovsky, I. Universal nonequilibrium properties of dissipative Rydberg gases. *Phys. Rev. Lett.* **113**, 210401 (2014).

38. Lesanovsky, I. & Garrahan, J. P. Out-of-equilibrium structures in strongly interacting Rydberg gases with dissipation. *Phys. Rev. A* **90**, 011603 (2014).

39. Urvoy, A. et al. Strongly correlated growth of Rydberg aggregates in a vapor cell. *Phys. Rev. Lett.* **114**, 203002 (2015).

40. Ding, D.-S. et al. Enhanced metrology at the critical point of a many-body Rydberg atomic system. *Nat. Phys.* **18**, 1447 (2022).

41. Helmrich, S. et al. Signatures of self-organized criticality in an ultracold atomic gas. *Nature* **577**, 481 (2020).

42. Ding, D.-S., Busche, H., Shi, B.-S., Guo, G.-C & Adams, C. S. Phase diagram of non-equilibrium phase transition in a strongly-interacting Rydberg atom vapour. *Phys. Rev. X* **10**, 021023 (2020).

43. Wintermantel, T. M. et al. Unitary and nonunitary quantum cellular automata with Rydberg arrays. *Phys. Rev. Lett.* **124**, 070503 (2020).

44. Klocke, K., Wintermantel, T., Lochead, G., Whitlock, S. & Buchhold, M. Hydrodynamic stabilization of self-organized criticality in a driven Rydberg gas. *Phys. Rev. Lett.* **126**, 123401 (2021).

45. Gambetta, F. M., Carollo, F., Marcuzzi, M., Garrahan, J. P. & Lesanovsky, I. Discrete time crystals in the absence of manifest symmetries or disorder in open quantum systems. *Phys. Rev. Lett.* **122**, 015701 (2019).

46. Wadenpfuhl, K. & Adams, C. S. Emergence of synchronization in a driven-dissipative hot Rydberg vapor. *Phys. Rev. Lett.* **131**, 143002 (2023).

47. Ding, D. et al. Ergodicity breaking from Rydberg clusters in a driven-dissipative many-body system. *Sci. Adv.* **10**, eadl5893 (2024).

48. Wu, X. et al. Dissipative time crystal in a strongly interacting Rydberg gas. *Nat. Phys.* **20**, 1389 (2024).

49. Liu, B. et al. Higher-order and fractional discrete time crystals in Floquet-driven Rydberg atoms. *Nat. Commun.* **15**, 9730 (2024).

50. Liu, B. et al. Bifurcation of time crystals in driven and dissipative Rydberg atomic gas. *Nat. Commun.* **16**, 1419 (2025).

51. Liu, B. et al. Microwave seeding time crystal in Floquet driven Rydberg atoms. Preprint at arXiv preprint arXiv:2404.12180 (2024b).

52. Pan, L., Chen, X., Chen, Y. & Zhai, H. Non-hermitian linear response theory. *Nat. Phys.* **16**, 767 (2020).

53. Crippa, L., Budich, J. C. & Sangiovanni, G. Fourth-order exceptional points in correlated quantum many-body systems. *Phys. Rev. B* **104**, L121109 (2021).

54. Yoshida, T. & Hatsugai, Y. Correlation effects on non-hermitian point-gap topology in zero dimension: reduction of topological classification. *Phys. Rev. B* **104**, 075106 (2021).

55. Busche, H. et al. Contactless nonlinear optics mediated by long-range Rydberg interactions. *Nat. Phys.* **13**, 655 (2017).

56. Bariani, F., Goldbart, P. M. & Kennedy, T. Dephasing dynamics of Rydberg atom spin waves. *Phys. Rev. A* **86**, 041802 (2012).

57. Konotop, V. V., Yang, J. & Zezyulin, D. A. Nonlinear waves in PT-symmetric systems. *Rev. Mod. Phys.* **88**, 035002 (2016).

58. Fleischhauer, M., Imamoglu, A. & Marangos, J. P. Electromagnetically induced transparency: optics in coherent media. *Rev. Mod. Phys.* **77**, 633 (2005).

59. Jiles, D. C. & Atherton, D. L. Theory of ferromagnetic hysteresis. *J. Magn. Magn. Mater.* **61**, 48 (1986).

60. Ogden, R. Elasticity and inelasticity of rubber. In *Mechanics and Thermomechanics of Rubberlike Solids* (eds. Saccomandi, G. & Raymond, W. O.) 135–185 (Springer, 2004).

61. Bergholtz, E. J., Budich, J. C. & Kunst, F. K. Exceptional topology of non-hermitian systems. *Rev. Mod. Phys.* **93**, 015005 (2021).

62. Zhang, X., Jin, L. & Song, Z. Dynamic magnetization in non-hermitian quantum spin systems. *Phys. Rev. B* **101**, 224301 (2020).

63. Qian, J. & Zhang, W. Dissipation-sensitive multiphoton excitations of strongly interacting Rydberg atoms. *Phys. Rev. A* **90**, 033406 (2014).

64. de Melo, N. R. et al. Intrinsic optical bistability in a strongly driven Rydberg ensemble. *Phys. Rev. A* **93**, 063863 (2016).

65. Dudin, Y. & Kuzmich, A. Strongly interacting Rydberg excitations of a cold atomic gas. *Science* **336**, 887 (2012).

66. Maxwell, D. et al. Storage and control of optical photons using Rydberg polaritons. *Phys. Rev. Lett.* **110**, 103001 (2013).

Acknowledgements

Author contributions

D.-S.D. conceived the idea with discussion from E.Z.L. J.Z., and Y.J.W. conducted the physical experiments, analysed the data with the assistance of B.L., L.-H.Z., Z.-Y.Z., S.-Y.S., Q.L., H.-C.C., Y.M., T.-Y.H., Q.-F.W., J.-D.N., Y.-M.Y., D.-Y.Z., G.-C.G., and B.-S.S. D.-S.D. and E.Z.L. developed the theoretical model. The manuscript was written by D.-S.D., J.Z., E.Z.L., and Y.J.W. The research was supervised by D.-S.D. All authors

contributed to discussions regarding the results and the analysis contained in the manuscript.

Competing interests

The authors declare no competing interests.

Additional information

Supplementary information The online version contains supplementary material available at https://doi.org/10.1038/s41467-025-58850-y.

Correspondence and requests for materials should be addressed to Dong-Sheng Ding.

Peer review information *Nature Communications* thanks the anonymous reviewer(s) for their contribution to the peer review of this work. A peer review file is available.

Reprints and permissions information is available at http://www.nature.com/reprints

Publisher's note Springer Nature remains neutral with regard to jurisdictional claims in published maps and institutional affiliations.